Rapid acoustofluidic mixing by ultrasonic surface acoustic wave-induced acoustic streaming flow

Beomseok Cha [a], Song Ha Lee [a], Syed Atif Iqrar [b], Hee-Gyeong Yi [c,d], Jangho Kim [c,d], Jinsoo Park [a,*]

[a] Department of Mechanical Engineering, Chonnam National University, Gwangju 61186, Republic of Korea
[b] College of Engineering and Physical Sciences, Aston Institute of Photonic Technologies, Aston University, Birmingham B4 7ET, United Kingdom
[c] Department of Convergence Biosystems Engineering, College of Agriculture and Life Sciences, Chonnam National University, Gwangju 61186, Republic of Korea
[d] Interdisciplinary Program in IT-Bio Convergence System, Chonnam National University, Gwangju 61186, Republic of Korea

ABSTRACT

Ultrasonic surface acoustic wave (SAW)-induced acoustic streaming flow (ASF) has been utilized for microfluidic flow control, patterning, and mixing. Most previous research employed cross-type SAW acousto-microfluidic mixers, in which the SAWs propagated perpendicular to the flow direction. In this configuration, the flow mixing was induced predominantly by the horizontal component of the acoustic force, which was usually much smaller than the vertical component, leading to energy inefficiency and limited controllability. Here, we propose a vertical-type ultrasonic SAW acousto-microfluidic mixer to achieve rapid flow mixing with improved efficiency and controllability. We conducted in-depth numerical and experimental investigations of the vertical-type SAW-induced ASF to elucidate the acousto-hydrodynamic phenomenon under varying conditions of total flow rate, acoustic wave amplitude, and fluid viscosity conditions. We conducted computational fluid dynamics simulations for numerical flow visualization and utilized micro-prism-embedded microchannels for experimental flow visualization for the vertical SAW-induced ASF. We found that the SAW-induced vortices served as a hydrodynamic barrier for the co-flow streams for controlled flow mixing in the proposed device. For proof-of-concept application, we performed chemical additive-free rapid red blood cell lysis and achieved rapid cell lysis with high lysis efficiency based on the physical interactions of the suspended cells with the SAW-induced acoustic vortical flows. We believe that the proposed vertical-type ultrasonic SAW-based mixer can be broadly utilized for various microfluidic applications that require rapid, controlled flow mixing.

1. Introduction

Rapid and controllable mixing of fluids at the microscale level is a fundamental operation in various biological and chemical assays, including chemical synthesis [1,2], biochemical reactions [3,4], and biomedical sample activation [5,6]. Compared to conventional mixing techniques, microfluidic mixing provides exceptional advantages including rapid heat and mass transfer, high homogeneity, and easy parallelization due to high surface area-to-volume ratio, precise and automated control, and miniaturization [7,8]. The low Reynolds number flows inside microchannels render the microfluidic flow mixing challenging as molecular diffusion is dominant over advection in mass transfer. The microfluidic mixers have been developed largely in two types: passive and active approaches. Passive micromixers rely on internal hydrodynamic forces to induce enhanced diffusion or chaotic advection based on the microchannel geometries or heterogeneous microstructures [9,10]. Despite their simplicity, a few inherent constraints still remain, including heavy dependence on fluid properties and flow rates, relatively long mixing time required, and large footprints [7,11,12]. In particular, the diffusive mixing time is significantly prolonged for high-viscosity fluids [13]. These limitations hamper the use of high-viscosity fluids for practical applications, including biochemical synthesis, disease detection, and cell lysis using colloids, sputum, and blood, which have relatively high viscosity [14–16]. On the other hand, active micromixers employ external forces, such as electric and magnetic fields, to achieve rapid and effective mixing [17–19]. As these field-assisted approaches require labeled fluids, such as electrical polarity or magnetic properties, they accompany inevitable restraints of

limited applicability and mixing efficiency that heavily depends on the fluid properties [7,12,18,20].

Recently, acousto-microfluidic mixers have been proposed to address the limitations of previous micromixers [21,22]. The acoustic approaches utilized acoustic streaming flow (ASF) for mixing, which derives from the attenuation of acoustic waves leading to momentum flux within the fluid [23]. The acoustofluidic mixing techniques have been widely developed being incorporated not only with microchannel but also with sessile droplets [24,25] or various geometrical channels [26,27] for the enhancement of mixing effect and their practical applications. The ASF can be mainly categorized as Rayleigh-Schlichting streaming and Eckart streaming. The Rayleigh-Schlichting streaming is induced by the boundary-driven streaming resulting from the wave attenuation near the no-slip solid boundary regime. The boundary streaming within the viscous boundary layer induces counter-rotating flow in the outer boundary region, consecutively resulting in periodic patterns of micro-vortices within the fluid [28]. These micro-vortices of acoustic streaming require high power consumption as the loss of acoustic energy is relatively greater near the viscous boundary, and the vortex regime is small, typically less than the acoustic wavelength, which could be unfavorable for fluid mixing [23,29]. On the other hand, Eckart streaming is a vortex-like flow propelled by the acoustic jet, resulting from the propagation of the acoustic wave and its acoustic pressure gradient in the fluid [30]. The acoustic momentum flow drives the fluid with a spatial dispersal along the direction of wave propagation, such that the acoustic streaming is generated in a larger scale of wave attenuation length [23]. A typical example of Eckart streaming is an ultrasonic surface acoustic wave (SAW)-based acoustofluidic mixer, which is based on the attenuation of the traveling SAWs for mixing. Most previous studies have predominantly employed cross-type SAW-based micromixers, where the SAWs propagate from the sidewall of the microchannel towards the fluids, resulting in the SAW propagation perpendicular to the flow [31–33]. In this case, as the leaky waves refracted into the fluid at the Rayleigh angle ($\theta_R \approx 22°$ in the water/LiNbO$_3$ interface), the vertical component of the ASF was approximately 2.5 times greater than the horizontal component [34]. Since the mass transfer required for mixing relied on the horizontal component of the SAW-induced ASF, the mixing efficiency was limited. In our earlier study, we introduced a vertical-type SAW-based micromixer to enhance the mixing efficiency, where the SAW-generating transducer was located underneath the microchannel such that the SAWs propagated parallel to the flow, and achieved homogeneous ($> 90\%$ mixing efficiency) and high-throughput (50 μl/min total flow rate) mixing with low power consumption (< 12 V$_{pp}$) [35]. However, in the absence of the in-depth quantitative investigations, the physical mechanism underlying the vertical SAW-induced ASF for flow control and mixing has not been elucidated yet.

Here we propose a vertical-type ultrasonic SAW-based micromixer to achieve rapid, uniform, on-demand, and controlled flow mixing for the potential biological application of chemical additive-free cell lysis at high-throughput. The SAW-generating interdigital transducer (IDT) was positioned right beneath the microchannel, allowing a direct propagation of ultrasonic waves to the working fluid and utilizing both vertical and horizontal acoustic components with high efficiency. For elucidation of the acousto-hydrodynamic phenomenon, we conducted thorough numerical and experimental investigations of the SAW-induced ASF under varying conditions of total flow rate, acoustic wave amplitude, and fluid viscosity. We conducted computational fluid dynamics simulations based on a wave attenuation model for numerical flow visualization and utilized micro-prism-embedded microchannels for experimental flow visualization of the vertical SAW-induced ASF for the first time. We found that the SAW-induced vortices served as a hydrodynamic barrier for the co-flow streams for controlled flow mixing in the proposed device. Based on the findings, we conducted a proof-of-concept demonstration for the ASF-induced chemical additive-free cell lysis at high-throughput and validated its potential to be utilized for

biological applications. We think that the proposed vertical-type ultrasonic SAW-based acousto-microfluidic mixer can be applicable to a variety of microfluidic applications that require rapid, controlled flow mixing.

2. Methodology

2.1. Device configuration and operation

Fig. 1 represents the device configuration of the proposed vertical-type ultrasonic SAW-induced acoustofluidic mixer. The device comprised a piezoelectric LiNbO$_3$ substrate with Cr/Au patterned IDT, and a SiO$_2$ layer was deposited on the substrate to protect the electrodes and enhance bonding between the substrate and the microchannel. A straight polydimethylsiloxane (PDMS) microchannel with two serial inlets and one outlet was bonded on the substrate via oxygen plasma treatment such that the IDT is located directly beneath the microchannel. Bidirectional SAWs propagation was aligned parallel to the flow direction, and the leaky longitudinal waves (LWs) refracted vertically into the fluid at the Rayleigh angle of approximately 22°. Rayleigh-type SAWs were produced from the IDT by the inverse piezoelectric effect when an AC signal with the resonant frequency of the IDT was applied to the transducer. We designed the IDT with the electrode spacing ($\lambda/4$) of 6.5 μm, whose corresponding resonant frequency (f) was approximately 153 MHz. Two fluids, fluid A as the sample and fluid B as the sheath, were introduced through two inlets with a volumetric flow ratio of 1:4. The injected fluids flowed in the form of vertically up-down double layers, as the fluid B pinched the fluid A downwards along with the upper streamlines. For the visualization of these double-layered fluids, a micro-prism was placed right next to the microchannel as a reflecting mirror of the optical path, and light-reacting compounds were dyed in each fluid; the fluid A absorbed the light with indelible ink or erioglaucine disodium salt, and the fluid B reflected the light with rhodamine B. The laser, as a light source, introduced through the inverted microscope was reflected off a 45° tilted mirror plane in a micro-prism to expose the side wall of the microchannel [36]. Each fluid represented a dark and bright field, as the compounds respectively absorbed and reflected the light reflected from the prism. Based on the device and experimental configuration, the vertically induced ASF can be visualized from the side view of the microchannel, which presents the span-wise of the streaming.

2.2. Working mechanism

Acoustic streaming is an acousto-hydrodynamic phenomenon that occurs due to the presence of a gradient in the time-averaged acoustic momentum flux within a fluid [23,30]. The ultrasonic SAWs produced from the IDT refract in the form of LWs and gradually attenuate, resulting in oscillating displacements in the working fluid. This wave attenuation-induced energy dissipation is transferred to the momentum flux in the fluid, which accelerates the fluid in the direction of LW propagation, inducing net fluid motion inside the microchannel [5,37]. For the numerical flow visualization of the ASF, we utilized the theoretical wave attenuation model, which incorporated the attenuation motion by time averaging over the excitation period of the wave as a form of time-averaged acoustic body force [23,38,39]. The wave attenuations along the substrate–fluid interface and in the fluid are first analyzed for the acoustic body force calculation [39]. The attenuation coefficient along the piezoelectric substrate and the fluid is defined as $\alpha = \rho_f c_f / \rho_s c_s \lambda_s$, where ρ_s is the substrate density, c_s is the speed of sound in the substrate, and λ_s is the acoustic wavelength in the substrate. The attenuation coefficient in the fluid is defined as $\beta = (4\mu/3 + \mu')\omega^2 / \rho_f c_f^3$, where μ and μ' are the dynamic and bulk viscosities of the fluid, respectively, ω is the angular frequency, and c_f is the speed of sound in the fluid. Assuming that the contribution of the shear wave is negligible owing to the comparatively low speed of sound in the fluid, the non-
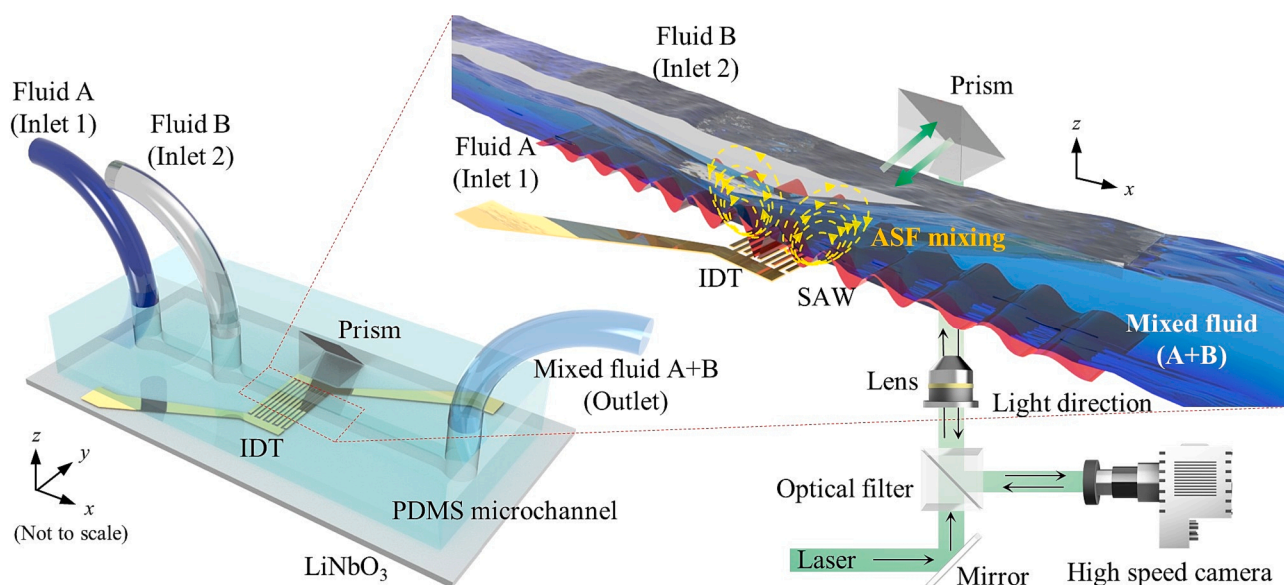
Fig. 1. Schematic of the acoustofluidic micromixer and working mechanism and the process of flow visualization of the side-view perspective from the micro-prism.

linear acoustic body force (F_{ASF}) induced at the (x, z) plane can be modeled as $F_{ASF} = \rho_f \beta u(x, z)^2$, where $u(x, z) = \omega \xi(x, z)$ is the displacement velocity with the displacement magnitude of the oscillation $\xi(x, z)$ [32,39]. Considering the first-order approximation of the wave reflection at the microchannel roof, the wave displacement magnitude can be expressed as $\xi(x, z) = \xi_0 (e^{-\alpha(x-z\tan\theta r)}e^{-\beta z\sec\theta r} + R_1 e^{-\alpha(x-(h-z)\tan\theta r)}e^{-\beta(h-z)\sec\theta r})$, where ξ_0 is the initial displacement of the acoustic waves, h is the height of the microchannel, and R_1 is the reflection coefficient. The coefficient R_1 is defined as $R_1 = ((Z_2 - Z_1)/(Z_1 + Z_2))^2$, where the acoustic impedance $Z_i = \rho_i c_i$ and the subscripts 1 and 2 represent the fluid/microchannel roof or fluid/substrate interfaces [39]. We geometrically designed the fluid domain of 600 μm-width, 160 μm-height, and 2000 μm-length in accordance with the microchannel and micro-prism which were experimentally used. The time-averaged acoustic body force was applied in two opposite directions from the center of the modeled microchannel scheme with boundary conditions including inlet flow rates and non-slip condition, as depicted in Supplementary Material (Fig. S1). The continuity equation combined with the Navier–Stokes equation is integrated with the time-averaged nonlinear acoustic streaming body force, expressed as $\rho_f(D\textbf{u}/Dt) = -\nabla P + \mu\nabla^2\textbf{u} + F_{ASF}$, and numerically solved using COMSOL Multiphysics 5.6.

3. Results and discussion

3.1. Numerical and experimental investigations of the vertical-type acoustic streaming flow

The proposed vertical-type ASF mixing approach is based on the enhanced magnitude of the micro-vortices in the ASF, which is induced by fully utilizing both vertical and horizontal components of the wave attenuation. The intensity of acoustic energy is proportional to the wave amplitude, which has a linear relationship with the voltage applied to the IDT as that $\xi_0^2 \sim V_{rms}^2$ where ξ_0 represents the initial amplitude of the SAW [40]. For a thorough evaluation of the vertical-type ASF, we conducted both numerical and experimental investigations using the wave attenuation model and the micro-prism-based flow visualization, respectively. Fig. 2(a) shows the two-dimensional (xz-plane) velocity field of the SAW-induced ASF and its vorticity field under varying wave amplitude of $\xi_0 = 0$–375 pm. Without acoustic field $\xi_0 = 0$ pm, the vertically parallel flow with a constant total flow rate ($Q_{tot} = 50$ μl/min) retained the original laminar flow streams. As the wave amplitude applied in the middle of the microchannel increased to $\xi_0 = 125$ and 250 pm, the flow gradually began to be deflected from bottom to top. An accelerated flow propulsion in the straight diagonal direction was induced with a sufficient wave amplitude of $\xi_0 = 375$ pm, such that asymmetric counter-rotating vortices were consequently presented fully
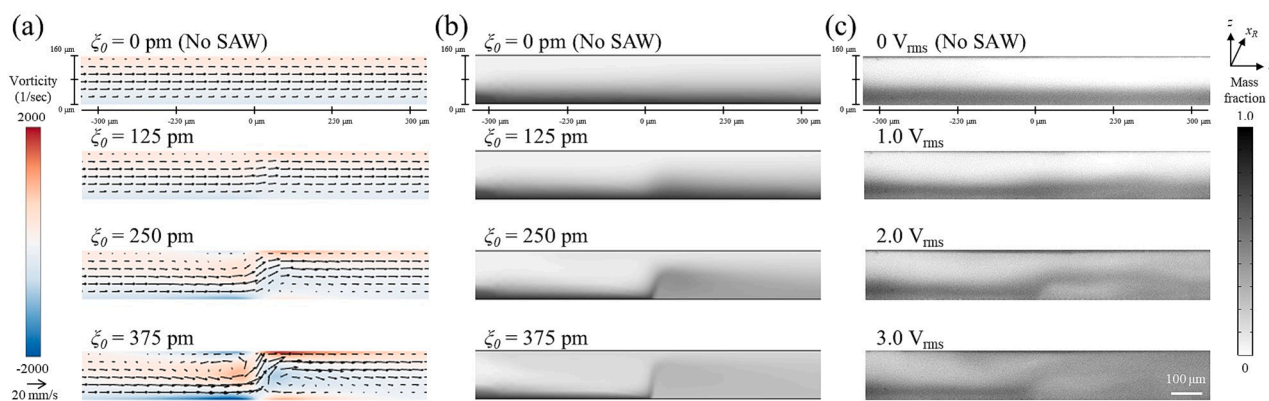

Fig. 2. Numerical simulation results of (a) two-dimensional vector fields and (b) the concentration profile at varying initial wave amplitudes and (c) the experimental cross-section flow visualization results at varying applied voltages.

covering the microchannel height. As the SAWs were produced and propagated in a bidirectional way from the IDT, a pair of momentum flux was also derived in a bidirectional way along the direction of wave propagation; one is in an equal direction and the other is in an opposite direction with the flow, respectively. The opposite-directionally induced acoustic momentum with relatively low wave amplitude ($\xi_0 = 125$ and 250 pm) was suppressed by the flow inertia, resulting in a slight deflection as a combination of the lateral flow and vertical acoustic momentum. The vertical velocity component of the ASF was significantly increased in accordance with the high wave amplitude ($\xi_0 = 375$ pm), leading to the accelerated propulsion acting as a hydrodynamic barrier against the initial lateral flow. The acoustic jet induced two vorticity regimes blocking the lateral flow direction and rotating with the deflection from the microchannel ceiling. We could expect an enhanced flow mixing from the symmetric vortices, as both positive and negative vorticities affect mixing in the backside and forward of the IDT, respectively. These numerical results also indicate that the two parallelly injected fluids could be controllably mixed by adjusting the intensity of ultrasonic energy.

For the in-depth observation of the mixing effect, diluted sample fluid mixing was conducted under the same conditions, both numerically and experimentally, as shown in Fig. 2(b) and (c), respectively. In the numerical simulation, the sample fluid was modeled to have a mass fraction of 1 whereas the sheath fluid had 0 mass fraction at a volumetric flow rate ratio of 1:4 and the total flow rate was 50 µl/min (Fig. S1). As shown in Fig. 2(b), the increased wave amplitude led to the bottom-pinched sample fluid flowing upwards and disturbing the fluid to be mixed owing to the interaction between the directions of inertia flow and the ASF-induced vortical flow. As also depicted in Supplementary Material (Fig. S2) with three-dimensional streamlines, we confirmed that enhanced mass transfer was achieved along the asymmetric counter-rotating vortices (Fig. 2(a) at $\xi_0 = 375$ pm), where the bottom-flowing solution was mixed to the entire height of the fluid domain. We could also compare the mixing efficiency of the two types of acousto-fluidic devices (cross-type ASF mixer and vertical-type ASF mixer) from the numerical simulation results. Under the same boundary conditions except for the direction of the acoustic body force, we confirmed that the concentration gradient of the sample fluid still remained with the cross-type ASF mixer (Fig. S3). The concentration gradient, on the other hand, was much lower for the vertical-type ASF mixer with the same wave amplitude ($\xi_0 = 375$ pm), which implied that mixing enhancement with high energy efficiency could be achieved by utilizing both vertical and horizontal acoustic components from the proposed vertical type acoustofluidic mixer. The preceding numerical simulations were compared and validated from the experimental flow visualizations captured from the micro-prism-assisted microscopy. The isopropyl alcohol (IPA) solutions, respectively dissolved with the indelible ink and the rhodamine B, were utilized as a sample fluid and a sheath fluid to clearly visualize the fluids interface. Fig. 2(c) shows the experimental results at the applied electrical voltage of 0–3.0 V_{rms}, which is proportional to the acoustic amplitude (see also Supplementary Movie 1). The fluids were injected into the microchannel at the total flow rate of 50 µl/min from the syringe pump. In the absence of the acoustic field condition (0 V_{rms}), the vertically layered parallel flow persisted over the unmixed laminar flow with a velocity of approximately 9.26 mm/s, similar to the numerical simulation ($\xi_0 = 0$ pm). As the vertical-layered fluids were exposed to the SAWs, the vertically induced momentum flux was observed, such that the bottom sample fluid deflected upwards with an acoustics-induced hydrodynamic barrier. Furthermore, there was an up-tilted concentration profile at 2.0 V_{rms}, with a relatively low concentration under the trace, which could be estimated from the presence of the small vortices with perturbations of the inertia incoming flow confirmed from the numerical results. When the applied voltage was approximately 3.0 V_{rms}, the two liquid solutions were completely mixed as they passed through the IDT, which was consistent with the results of the numerical simulation under the sufficient wave amplitude of 375 pm. We could

estimate that the asymmetric counter-rotating flow was induced within the flow, as the disturbance of the solution was formed in the vortices spatial regime in both numerical and experimental results ($\xi_0 = 375$ pm in Fig. 2(b), 3.0 V_{rms} in Fig. 2(c)). Notably in the experimental results of 3.0 V_{rms}, some concentration gradient was observed in the backward direction of the flow, indicating that the mass transfer was induced along with the counter-rotating ASF, consequently enhancing the mixing effect. The intensity of these vertically induced pair of vortexes could be also controllable with applied acoustic energy, which consequently induced not only enhanced mixing but also active-controlled concentration gradients along the fluid domain. This controllability could be utilized for engineering applications with mixing-based concentration control including biological tests [33] which might be unachievable with chaotic disturbance mixing [41]. Based on the numerical investigations, the flow mixing effect of the vertically induced ASF at varying intensities of ultrasonic wave amplitude can be predicted and validated using two-dimensional (2D) flow vector fields and diluted sample fluid mixing simulations. We could experimentally visualize the vertically induced ASF by utilizing micro-prism at varying applied voltages which were carefully chosen based on the linear-proportional relationship with the initial wave amplitude ($\xi_0^2 \sim V_{rms}^2$). These micro-prism-assisted flow visualizations were in good agreement with the numerically described ASF fields and the mixing phenomenon.

For quantitative evaluation of the ASF-based acoustofluidic mixing, we conducted additional experiments to examine the effect of wave amplitude and total flow rate on the micro-mixing induced by the vertical-type ASF. For the quantification of fluid mixing, we introduced a mixing index (M_i) calculated with gray value, which is proportional to the diluted concentration, of captured images, defined as $M_i = 1/C_c(\Sigma (C_j - C_c)/N_p)^{1/2}$ where C_c is the mean gray value under the completely mixed condition, C_j is the gray value in each pixel, and N_p is the total number of pixels in the affected region of ASF [42]. The calculated M_i was further normalized in the form of $M_{i,nor} = 1 - (M_i - M_f)/(M_0 - M_f)$, where M_f and M_0 are the values for the fully mixed and unmixed scenarios, respectively, to be expressed from 0 (unmixed) to 1 (completely mixed) [43]. We evaluated the normalized mixing index of varying $Q_{tot} = 50$–200 µl/min and applied voltages of 0–6.0 V_{rms}, as shown in Fig. 3 (a). Under a constant SAW intensity produced with an applied voltage of 4 V_{rms}, comparably low total flow rates (< 100 µl/min) of two injected fluids were mixed by the vertical-type ASF with high uniformity ($M_{i,nor} > 0.9$). The flow rates exceeding 100 µl/min associated with high inertia, in contrast, suppressed the acoustic momentum, resulting in decreased mixing effects ($M_{i,nor} < 0.7$). Considering the numerically calculated vector field of ASF under different ultrasonic intensities, we could infer that the acoustic body force inducing the ASF was hindered by the inertia force at a high flow rate. These observations indicated that the velocity of the ASF induced by the sufficient acoustic power density should be higher than the flow velocity driven by the flow rate for the presence of counter-rotating flow, which leads to acoustofluidic mixing. Fig. 3(b) represents the theoretically calculated displacement magnitudes in the fluid, decaying along the wave propagating direction in the fluid (x_R-direction), which is defined as $\xi_f(x_R) = \xi_0 e^{-\beta x_R}$ [39]. The higher wave amplitude ($\xi_0 = 375$ pm, red line) exhibited a greater spatial extent of oscillatory motion in comparison to the lower wave amplitude ($\xi_0 = 125$ pm, black line) in the fluid, indicating an enhanced intensity of the acoustic momentum and its wide affecting range.

Complete mixing ($M_{i,nor} \approx 1.0$) of the relatively high flow rate of 0.2 ml/min was achieved with an increased acoustic body force driven from 6.0 V_{rms} applied voltage, as a demonstration of the theoretical estimation. The flow rate of 50 µl/min is regarded as high relative to the cross-sectional area of the microchannel compared with previously proposed active micromixers [17,18,32,44]. However, our proposed device demonstrated enhanced mixing capabilities compared to the previous micromixers, achieving high uniformity mixing at significantly increased fluid velocity; an average flow velocity of approximately 30 mm/s at 0.2 ml/min. Moreover, the employment of the vertical-type

(a)

(b)

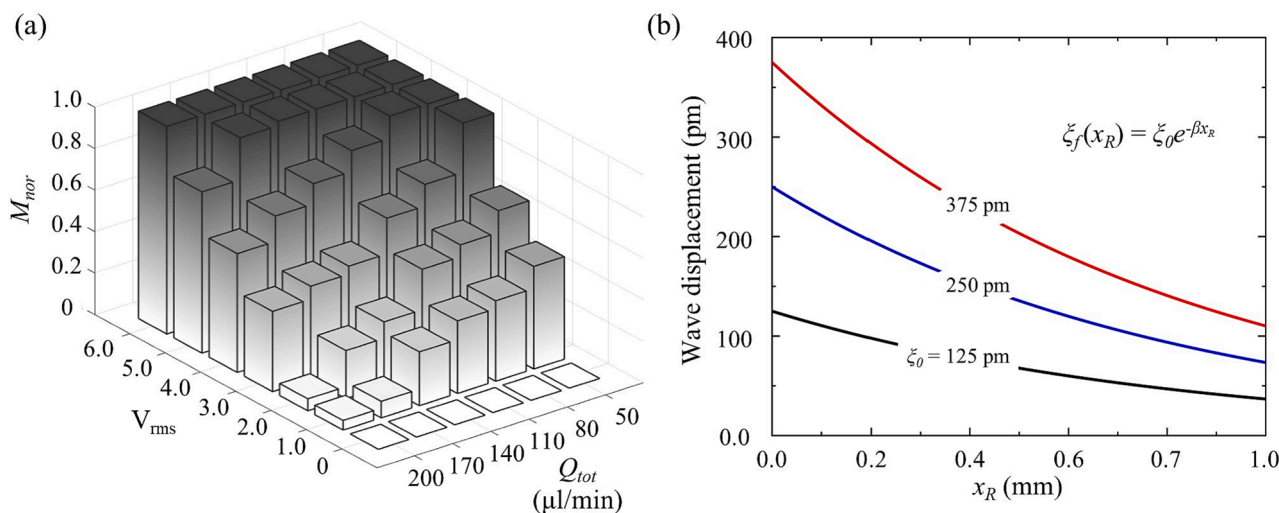
$$\xi_f(x_R) = \xi_0 e^{-\beta x_R}$$

Fig. 3. (a) A three-dimensional bar chart depicting the quantitative mixing index under various applied voltages proportional to wave amplitudes and to the total flow rates. (b) The displacement magnitudes of varying initial displacement in the fluid to the x_R direction, which is in parallel with the wave propagation in the fluid.

ASF mixer offered enhanced energy efficiency which could be achieved with the high utilization of vertical acoustic component. The applied voltage in the proposed device was relatively low (< 6 V_{rms}) in comparison to other platforms, such as the Rayleigh-Schlichting streaming-driven acoustic mixer and cross-type SAW acoustic mixer [21,45]. As the devices used to actuate the IDT including the connectors and cables have constant electrical impedance of 50 Ω and the gain power from the amplifier was 42 dBm, the range of applied power could be calculated from the conversion equations [46] and found to be approximately < 1.0 W. The frequency and microchannel dimensions utilized in this study were carefully chosen and designed considering the wave attenuation in the working fluid and its vertically inducing ASF. The wavelength in the fluid (λ_f) of the 153 MHz frequency was calculated at approximately 9.8 μm ($\lambda_f = c_f/f$). The height of the microchannel h was designed and fabricated to be 160 μm, such that sufficient acoustic damping to the vertical direction of the microchannel (from bottom to ceiling, as $h/\lambda_f \cos\theta_R > 15$) could lead to acoustic momentum propulsion with greater wave attenuation. We also evaluated the temperature increase accompanied by the utilization of acoustic energy, which can potentially damage biological samples in the fluid, consequently, limiting the practical applications of the acoustofluidic device [47]. The maximum temperature raised by acoustic activation was measured to be approximately 35°C, which is lower than the temperature of a human body (Fig. S4). We could estimate the temperature increase would yield to under 10°C, as the maximum temperature was measured at the extreme case of our experimental conditions (lowest flow rate of 50 μl/min with the highest applied voltage of 6 V_{rms}). This indicated that the heat generation from the proposed device could be ruled out for manipulating biological sample fluid. Based on the findings, the proposed acoustofluidic device validated the capabilities of controllable and high throughput mixing, thereby securing the applicability for the chemical and biological manipulation fields.

3.2. Viscosity effect on acoustic streaming flow

From a practical perspective, for biological applications, high-viscosity fluid mixing is essential; for example, human-derived liquids have higher viscosity compared to pure water (≈0.89 mPa·s), e.g., blood viscosity of approximately 3.5 mPa·s [48] and semen viscosity of approximately 9.35 mPa·s [49]. From this viewpoint, we elucidated the effect of fluid viscosity on the ASF and its mixing phenomenon. First, we predicted the effect of viscosity on the vertically induced ASF through numerical simulations at varying fluid viscosities of 1–10 mPa·s, where

the viscosity of most human-derived fluids for liquid biopsy including blood, urine, saliva, and semen. Fig. 4(a) depicts the 2D flow vector plots of the vertical ASF under constant total flow rate ($Q_{tot} = 50$ μl/min) and initial wave amplitude ($\xi_0 = 375$ pm). The Eckert streaming induced by vertical acoustic momentum flux was fully generated for fluids below the viscosity of approximately 3.0 mPa·s, with a relatively high velocity of the acoustic propulsion compared with the lateral flow velocity. With a viscosity increase beyond 4.0 mPa·s, however, a notable reduction in acoustic momentum transfer was observed, as the upward streaming motion induced by the vertical momentum component was overpowered by the inertia of the flow rate. The viscosity effect on the ASF mixing trend could be estimated from these two-dimensional ASF vector plots. As depicted in Fig. 4(b), the bottom pinched sample fluid in the low viscosity fluids (< 4 mPa·s) could be transferred to the overall microchannel with significantly diverted angles to the lateral flow direction. The concentration profiles of the diluted sample in this viscosity regime were in good accordance with the streamline vector (Fig. 4(a)). Here, the asymmetric counter-rotating ASF was completely dominant as an acoustic hydrodynamic barrier in a vertical direction blocking the lateral flow and mixing the two fluids. The mass fraction gradients were present after the ASF region with greater fluid viscosity (> 4 mPa·s), as a weaker hydrodynamic barrier of the acoustic jet led to the absence of the fully covering micro-vortices.

To confirm the numerically estimated acousto-hydrodynamic phenomenon, we performed repeated experiments and visualized the mixing phenomenon with varying dynamic viscosities of the fluid $\mu = 1.0–10$ mPa·s. The varying viscosities fluids were fabricated by changing the mixing ratio of the water and glycerol mixture solution [50], and each sample and sheath fluids were dissolved with erioglaucine disodium salt and rhodamine B, respectively for the micro-prism-assisted flow visualization. Under constant applied voltage (3.0 V_{rms}) of the actuating SAW and flow rate of 50 μl/min, double-layered fluid mixing of varying fluid viscosities was observed via the micro-prism, as shown in Fig. 4(c). The vertically induced ASF achieved the mass transfer and agitated flow mixing of the diluted sample fluids in the vertical direction by breaking the interface between the two parallel fluids with viscosities below 3.0 mPa·s. For viscosities < 8.0 mPa·s, on the other hand, the minor affecting of the vertical ASF resulted in the decreased mixing effect with reduced vorticities as predicted from 2D vector plots. The acousto-hydrodynamic barrier was observed at the deflected angle (6.0 mPa·s in Fig. 4(c)), as the diluted sample profile was slightly fluctuated in the acoustic momentum regime, indicating the presence of the micro vortices of the perturbations of lateral flow. This ultrasonic-induced
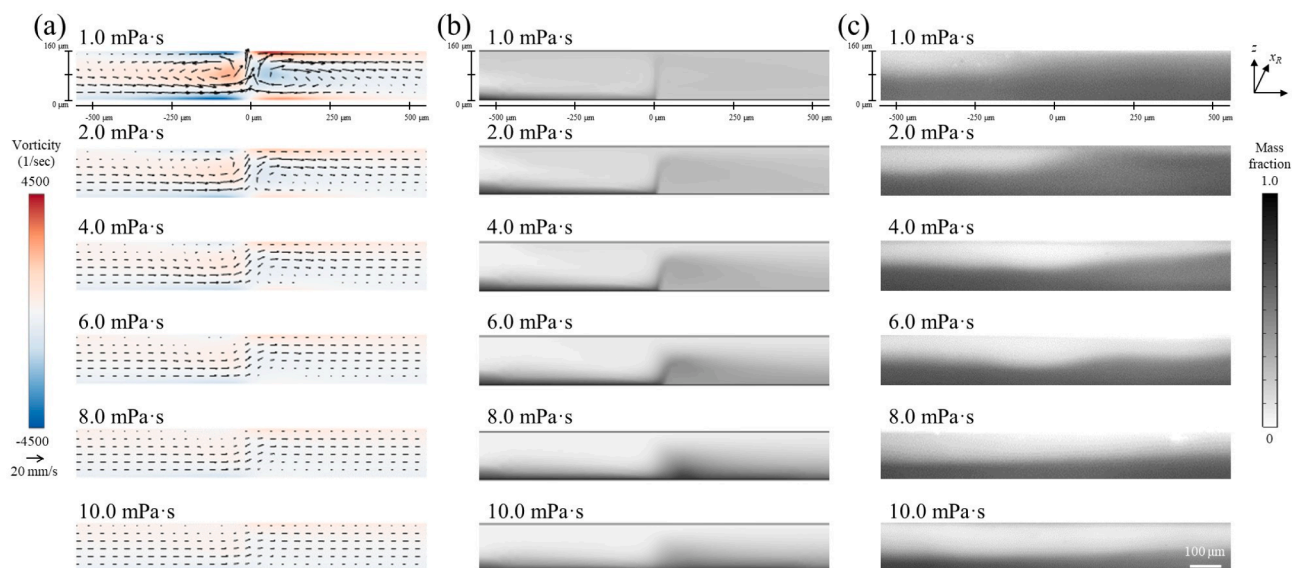
Fig. 4. Numerical simulation results of (a) 2D vector fields and (b) concentration profile and (c) the experimental cross-section flow visualization results at varying fluid viscosities.

hydrodynamic barrier was much powerless for the viscosities of 8.0 and 10 mPa·s, such that the bottom sample fluid only slightly deviated upwards while sustaining the vertical-layered separation. The acoustic jet could not penetrate the lateral flow inertia suggesting the reduced acoustic momentum was derived within the higher viscosity fluids, which was in line with the inclination of theoretical approaches (also shown in Supplementary Movie 2). Reminding the mechanism of the ASF and its theoretical model, the attenuation coefficients are the two key players of the acoustic body force: one is along the interface between the substrate and fluid (α), and the other one is in the fluid (β) [39]. As outlined in the previous methodology section, the theoretical wave attenuation model suggests that the attenuation coefficient in fluid β is directly proportional to the fluid viscosity, and the wave displacement magnitude follows a bi-exponential decay pattern that scales with the minus exponential of β ($\xi \sim e^{-\beta}$) [39]. In other words, we can consider that the longitudinal wave attenuation in the working fluid significantly decreases with an increase in fluid viscosity, which consequently reduces the oscillatory momentum transferred from the waves [51]. The experimental observations were well-matched with the numerically simulated results, validating that the acoustic momentum transfers

decreased as the viscosity of the working fluid increased.

Furthermore, as an in-depth investigation of the effect of fluid viscosity on ASF mixing, we quantified the mixing efficiency based on the flow visualization results. Under constant total flow rate (50 μl/min), we recorded the experimentally visualized ASF mixing at varying dynamic viscosities of 1–10 mPa·s and applied voltages of 0–5.0 V_{rms}, and calculated the normalized mixing index ($M_{i,nor}$). A 3D bar chart presented in Fig. 5(a) illustrates the quantitative evaluation of the mixing efficiency of viscous fluids driven by the vertical-type ASF. Here, we could remark the mixing trends, where the mixing index significantly varied with the changes in fluid viscosities and wave amplitudes. For fluids with viscosities over 4.0 mPa·s, the mixing process was found to be minimally impacted ($M_{i,nor} < 0.4$) by the ASF at low applied voltages ($<$ 2.0 V_{rms}). This observation can be explained by the reduction of acoustic momentum flux resulting from the theoretical inverse relationship between the spatial decaying wave magnitudes and the fluid viscosity. The decaying oscillatory motions of wave magnitudes in the fluids of varying viscosities further supported the numerical and experimental findings (Fig. 5(b)). The wave attenuation was theoretically calculated to be gradually decayed in the fluid with relatively low viscosity (1 mPa·s, in
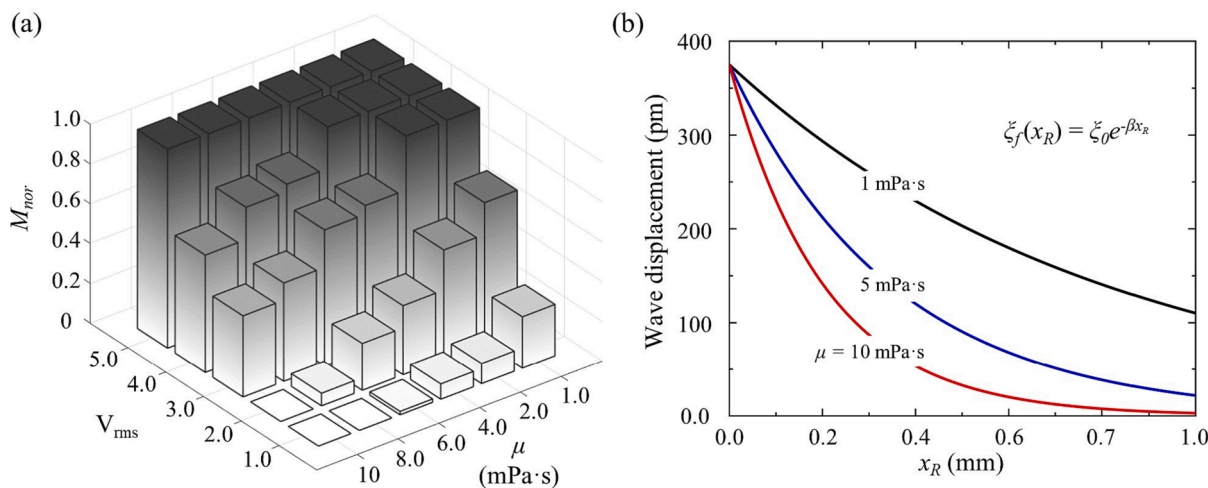

Fig. 5. (a) A 3D bar chart depicting the quantitative mixing index under various applied voltages proportional to wave amplitudes and fluid viscosity. (b) The displacement magnitudes in the fluid of varying viscosities to the x_R direction, which is in parallel with the wave propagation in the fluid.

black line), which could be consequently related to extended acoustic momentum transfer and acoustic streaming. The spatial extent of the oscillatory motions would sharply decay with the increased fluid viscosities, indicating the reduced acoustic body force regime and leading to the weakening of momentum flux in the working fluid (10 mPa·s, in red line). The numerical and experimental results were observed in the same trend as the theoretical calculations, thus confirming the effect of highly viscous fluids on the ASF and its mixing capabilities. The degree of fluid mixing, however, significantly increased for these fluids, as the acoustic body force was intensified by an applied voltage of 3.0 V_{rms}, and eventually reached saturation of $M_{i,nor} \approx 1.0$ when the applied voltage increased to 5.0 V_{rms}, indicating complete mixing. The results have revealed that the sufficient ultrasonic wave amplitude can be attributed to the enhanced acoustic momentum as compensation for the sharply decaying oscillation in the relatively high-viscosity fluids. The enhanced momentum transfer could overwhelm the viscosity effect, consequently inducing the disturbing ASF and high uniformity mixing of the fluids. As the effectiveness of the vertically induced ASF device in facilitating the mixing of viscous fluids has been demonstrated from both numerical and experimental findings, the proposed acoustofluidic micromixer has been validated for its applicability in practical engineering fields dealing with viscous fluids.

3.3. Acoustofluidic chemical-free cell lysis

Microfluidic mixing of viscosity fluids at high throughput has been widely utilized in broad applications, ranging from biochemical reactors and disease detection to cell lysis [4,14,16,33,52,53]. As a proof-of-concept demonstration of an investigation-based engineering appliance of microfluidic mixing, the vertical-type ASF micromixer was employed for a mechanical cell lysis platform. Cell lysis is a cell-disrupting process employed to release the cell contents, which is essential for detecting and diagnosing diseases, as the biomarkers are not detected on the exterior of the single cell membrane [53]. Previous strategies have realized cell lysis in chemical- or physical-rupturing manners [54]. Chemical-based lysis utilized surfactant to rupture the cell membrane, but this involved a high risk of denaturation of the cell/bio samples [55]. Physical-based lysis employed external forces to induce membrane rupture, thus limiting continuous processes such as point-of-care applications [56]. Recent previous studies have utilized the traveling SAW for cell lysis with continuous-flowing microfluidic devices [57,58]. These approaches were based on the cross-type of acoustic waves, which required high power consumption (~ 15.8 W) [57] and relatively low flow rate (250 μl/h) [58] with poor utilization of the vertical acoustic components. Here, we performed red blood cell (RBC) lysis using the proposed ultrasonic ASF micromixer in a chemical-free manner, expecting the precise controllability of the functionality based on our findings, and its applicability of diagnostics, such as malarial parasites, and integration of the downstream analysis devices. It should be noted that the proposed acoustofluidic technique is not limited to RBCs, although acoustofluidic chemical-free RBC lysis experiments were performed as a proof-of-concept demonstration. The proposed vertical ASF device aimed at inducing streaming-based physical interaction between individual cells or solid beads, resulting in the RBCs rupturing and releasing their enclosed contents. For validation of the device's capability to meet the goal, an RBC solution filtered from whole blood and a 6.1 μm polystyrene (PS) micro-bead diluted phosphate-buffered saline (PBS) solution were injected into each inlet of the configured device. An input voltage of 4.0 V_{rms} was applied to induce the vertical ASF under 50 μl/min flow rate, which was carefully chosen based on our findings (Fig. 4 and Fig. 5(b)) of viscous fluid mixing considering blood viscosity of approximately 3.5 mPa·s [48]. The microscopic images in Fig. 6(a) and (b) depict the morphological comparison of the RBCs before and after lysis, respectively. As shown in Fig. 6(a), un-lysed RBCs in the absence of ASF were spherical and reddish in shape, with enclosed hemoglobin. In contrast, the RBCs passed through the actuating ultrasonic ASF regime seemed to be lysed, presenting a transparent and blurred shape, as hemoglobin had leaked out from the ruptured RBC (Fig. 6(b)). The confirmation of un-lysed/lysed RBCs could be also visually verified by the precipitation of the RBCs [53,59]. The RBC solutions that penetrated the device without and with SAW were respectively collected in microtubes and centrifuged, as presented in Fig. 6(c). The sample fluid untreated by SAW was clearly separated into precipitated RBCs and buffer, implying no leakage of hemoglobin from the RBCs. The ultrasonic SAW-treated sample fluid, however, appeared reddish with the uncertain interface between the RBCs and buffer solution, suggesting that the hemoglobin had been released from the ruptured RBCs [59]. These visible observations implied that the vertically induced ASF mixing caused sufficient physical interactions on the RBCs, leading to cell lysis.

We further quantitatively verified the ASF-mixing-driven RBC lysis by measuring the removal of hemoglobin via ultraviolet–visible spectroscopy (UV–vis). Three representative absorption peaks of hemoglobin at λ = 412, 543, and 577 nm were observed from the untreated RBCs, thus confirming their un-lysed state, as shown in Fig. 7(a) and depicted as a red line [60,61]. For the PBS-diluted RBC solution, the absorption peaks remained despite their decreased intensity owing to dilution (black line). The RBC solution lysed by ASF mixing, in contrast, showed approximately 90% decreased absorption peaks compared with the original RBC solution, indicating the loss of hemoglobin (blue line). We thus verified that the RBCs were successfully lysed by applying vertically induced ASF mixing, despite the presence of a slight remaining signal, which may have been caused by the remnants from the RBC washing process [60]. For the quantitative characterization of the effect of ASF mixing on RBC lysis, we conducted additional experiments to evaluate the mixing efficiency at varying intensities of the ASF. Not only a PS-bead-diluted PBS solution but also PBS solutions without other compositions were utilized as the sheath fluid for an in-depth investigation of the effect of ASF on physical interaction during cell lysis. The RBC lysis efficiency of ultrasonic ASF mixing was calculated by $(N_{lysed}/N_{tot}) \cdot 100$,
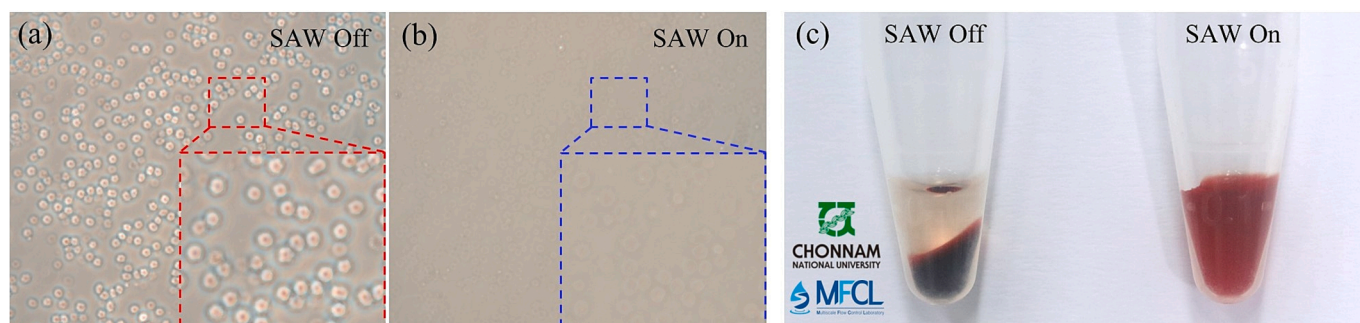

Fig. 6. Optical microscope images of RBCs (a) in the absence and (b) in the presence of the SAW and (c) the precipitated solutions obtained by centrifugation for each sample.
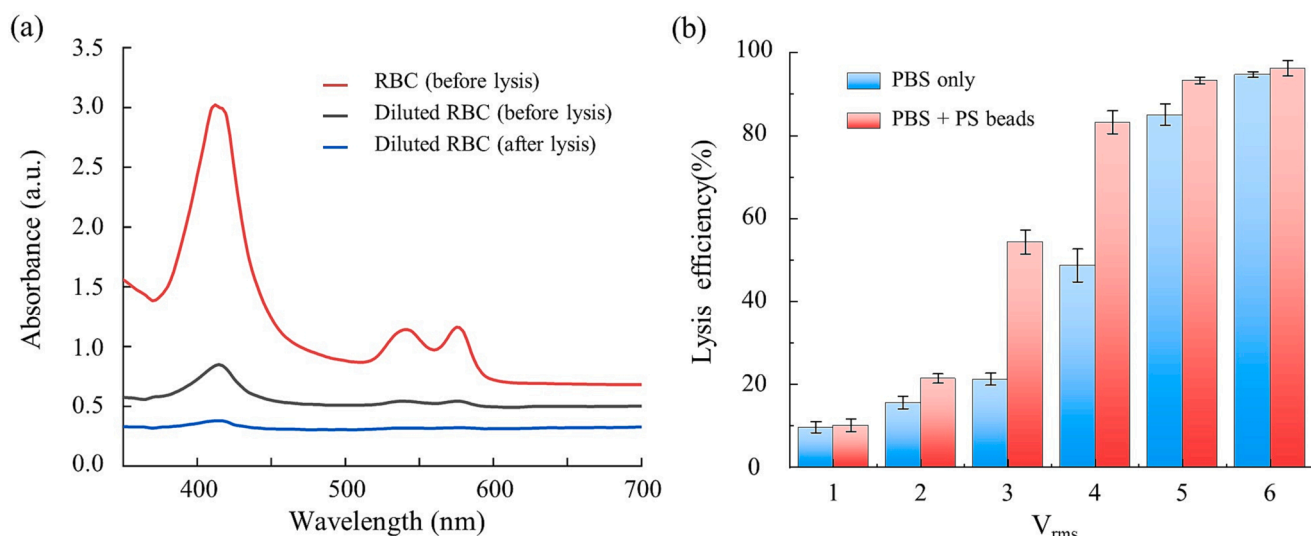
Fig. 7. (a) UV–vis spectrum of RBC, diluted RBC, and ASF-based lysed RBC. (b) RBC lysis efficiency for PBS-based lysis and PS-bead-diluted PBS solution–based lysis at varying applied voltages.

where N_{lysed} is the number of lysed cells, and N_{tot} is the total number of cells in the captured microscopic images from repeated experiments (n $\geq$ 3). Fig. 7(b) shows the efficiency of the ASF-driven RBCs lysis at varying voltages of 0–6.0 V_{rms} and a constant total flow rate (50 µl/min). The results presented that for both cases of sheath fluids, the lysis efficiency was increased in accordance with increasing applied voltage, which is proportional to the ASF intensity (also shown in Fig. S5). The experimental findings indicated that the mechanical stress induced by ASF-driven agitation was the primary factor affecting the cell lysis; this finding was further supported by the high similarity of the mixing effect evaluation at varying applied voltages (Fig. 5(b)). In addition, we confirmed that the lysis efficiency was significantly improved in the presence of PS beads in the mixing solution, which led to the reinforced physical collision with the cells. Nevertheless, a mixing efficiency of > 90% was achieved regardless of the presence of PS beads at a sufficient applied voltage of 6.0 V_{rms}, which induced high velocity and vorticity of the vertical ASF. In other words, controllable as well as high lysis efficiency can be achieved in a chemical-free, continuous, and tunable manner by tuning the intensity of ASF mixing with the driving voltages. Our findings demonstrated the potential of the proposed ultrasonic ASF-driven micromixer for practical biomedical applications owing to its high throughput and high viscosity mixing of blood.

4. Experimental

The IDT comprising bimetallic electrodes with Cr/Au (30 nm/100 nm) was deposited onto a piezoelectric $LiNbO_3$ substrate (128° Y-X cut, 0.5-mm thick, 4-inch diameter, MTI Korea) via the e-beam evaporation process. The IDT was designed to induce SAWs of approximately 153 MHz with comb-shaped electrodes spacing ($\lambda/4$) of 6.5 µm; it comprises 1.5 mm total aperture and 30 pairs of electrodes. A 200 nm SiO_2 layer was deposited onto the $LiNbO_3$ substrate via photolithography and reactive ion etching techniques to enhance the bond between the substrate and microfluidic chip as well as to prevent the electrodes from the environment. The micro-prism–embedded microfluidic chip was fabricated via soft lithography using the prism-locating microchannel mold. The microchannel mold with the prism aligner was designed not only for fabricating the microchannel (12 mm in length and 600 µm in width) but also as the micro-prism locating guide. The micro-prism aligner is in an L-shape structure that positions a 2 mm × 2 mm micro-prism (N-BK7 Right Angle Prism, Edmund Optics Worldwide) away from the sides of the microchannel. During the soft lithography process, the micro-prism was placed in the aligner prior to the casting of PDMS (Sylgard 184A and

184B, Dow Corning) and subsequently embedded as the PDMS cured. Following the fabrication of the prism-embedded microchannel, the microfluidic chip was bonded to the substrate via oxygen plasma treatment (Covance, Femto Science), thus aligning the center of the microchannel and the IDT. The IDT was actuated by an RF analog signal generator (N9310A, Keysight Technologies), a DC power supply (EX50-24, ODA Technology), and a high-power amplifier (ZHL-100 W-GAN+, Mini-Circuit). The input voltage applied to the IDT was measured by an oscilloscope (MSOX4154A, Keysight Technologies).

To enhance the clearance of the layered co-flow interface, we used an indelible ink (STSG-1 Black, Shachihata) and erioglaucine disodium salt (Sigma Aldrich) solution as the sample fluid, and the sheath fluid was composed of a solution of rhodamine B (Sigma Aldrich). For the investigation of the vertical-type ASF and its mixing effect, 30 µl of indelible ink was blended with 20 ml of IPA, and rhodamine B was dissolved in IPA to obtain a 50 µM solution. The fluids were injected under varying flow rates of 50–200 µl/min using multichannel syringe pump (neM-ESYS, Cetoni GmbH). To evaluate the effect of viscosity, 20 mg of erioglaucine disodium salt was diluted in viscous fluids composed of water–glycerol mixture, as the indelible ink is not soluble in water, and the rhodamine B solution in the water–glycerol mixture was the same with 50 µM. The experimental flow visualizations were captured by a high-speed camera (VEO 710L, Phantom Ametek) mounted on a light microscope (IX73, Olympus) through an objective lens (UplanFL 10X, Olympus) at 24 fps. The captured images of the mixing phenomenon were analyzed using ImageJ software (https://rsb.info.nih.gov/ij).

For the RBC lysis experiment, human RBC solution was purchased from Korean Red Cross (Republic of Korea), and diluted PBS solution was used as a buffer solution. Ethics approval for experiments reported in the submitted manuscript on animal or human subjects was granted. This study was approved by the Institutional Review Board of the Chonnam National University (IRB No. 1040198-210701-BR-099-03). We utilized 6.1 µm PS solution (1% w/w) (Duke Scientific) as a collisional particle, whose size was carefully chosen in comparison to the size of RBC, as the cells could not be ruptured with the relatively small size of beads and could be trapped among the larger size of beads [62]. Because RBCs can be lysed by water owing to osmotic pressure, we precipitated 1 ml of PS solution and removed the supernatant to prepare PBS-diluted PS solution. The precipitated micro-beads were dissolved in 2.5 ml of PBS, and the solution was utilized for RBC lysis. The lysed RBC solution was washed three times, repeating the precipitation and dilution with 1 × PBS solution for UV–vis analysis. The baseline on the UV–vis spectrophotometer (OPTIZEN POP, KLAB) was set using 1 × PBS solution,

and the spectrum peaks were measured for each sample.

5. Conclusions

In this study, we developed an acousto-microfluidic mixer based on the vertical-type SAW-induced ASF. The IDT, from which the ultrasonic SAWs were generated, was located right beneath the microchannel, leading to improved energy efficiency and controllability. We conducted thorough numerical and experimental investigations of the vortical flow structures induced by the vertical-type SAWs under varying fluid, flow, and acoustic conditions to elucidate the working mechanisms underlying acosuto-hydrodynamic phenomenon. From the numerical and experimental flow visualizations, the vertically induced acoustic momentum flux was observed to derive a pair of asymmetric micro-vortices that served as an acousto-hydrodynamic barrier for flow control and mixing. We achieved rapid, controlled flow mixing at low power (< 6.0 V_{rms}) and high throughput (~ 0.2 ml/min) with viscous fluids (~ 10 mPa·s). We further demonstrated chemical-free acousto-microfluidic cell lysis at high throughput. The lysed RBCs were visibly and quantitatively verified, and in-depth characterization of lysis efficiency was conducted under a controllable intensity of the ASF mixing. Consequently, not only high lysis efficiency ($> 90\%$) but also controllable lysis could be realized in a chemical-free and continuous manner. Based on the findings, we expect that the proposed vertical-type ultrasonic ASF micromixer is a promising approach for microfluidic mixing and can be employed in various chemical and biomedical applications.

CRediT authorship contribution statement

Beomseok Cha: Validation, Formal analysis, Investigation, Writing – original draft, Writing – review & editing. **Song Ha Lee:** Formal analysis, Investigation, Writing – review & editing. **Syed Atif Iqrar:** Investigation, Writing – review & editing. **Hee-Gyeong Yi:** Investigation, Writing – review & editing. **Jangho Kim:** Investigation, Writing – review & editing. **Jinsoo Park:** Conceptualization, Methodology, Validation, Formal analysis, Writing – original draft, Writing – review & editing, Supervision, Funding acquisition.

Declaration of Competing Interest

The authors declare the following financial interests/personal relationships which may be considered as potential competing interests: Jinsoo Park reports financial support was provided by National Research Foundation of Korea. Jinsoo Park reports equipment, drugs, or supplies was provided by Energy Convergence Core Facility in Chonnam National University.

Acknowledgments

Appendix A. Supplementary data

Supplementary data to this article can be found online at https://doi.org/10.1016/j.ultsonch.2023.106575.

References

[1] Y. Song, J. Hormes, C.S. Kumar, Microfluidic synthesis of nanomaterials, Small 4 (2008) 698–711.
[2] S. Yang, F. Guo, B. Kiraly, X. Mao, M. Lu, K.W. Leong, T.J. Huang, Microfluidic synthesis of multifunctional Janus particles for biomedical applications, Lab Chip 12 (2012) 2097–2102.
[3] G.M. Whitesides, The origins and the future of microfluidics, Nature 442 (2006) 368–373.
[4] Y. Xie, D. Ahmed, M.I. Lapsley, S.-C. Lin, A.A. Nawaz, L. Wang, T.J. Huang, Single-shot characterization of enzymatic reaction constants K m and k cat by an acoustic-driven, bubble-based fast micromixer, Anal. Chem. 84 (17) (2012) 7495–7501.
[5] S. Kim, H. Nam, B. Cha, J. Park, H.J. Sung, J.S. Jeon, Acoustofluidic stimulation of functional immune cells in a microreactor, Adv. Sci. 9 (2022), 2105809.
[6] X. Mu, W. Zheng, J. Sun, W. Zhang, X. Jiang, Microfluidics for manipulating cells, Small 9 (2013) 9–21.
[7] C.-Y. Lee, C.-L. Chang, Y.-N. Wang, L.-M. Fu, Microfluidic mixing: a review, Int. J. Mol. Sci. 12 (2011) 3263–3287.
[8] Y. Liu, X. Jiang, Why microfluidics? Merits and trends in chemical synthesis, Lab Chip 17 (23) (2017) 3960–3978.
[9] A.D. Stroock, S.K.W. Dertinger, A. Ajdari, I. Mezić, H.A. Stone, G.M. Whitesides, Chaotic mixer for microchannels, Science 295 (5555) (2002) 647–651.
[10] Y.K. Suh, S. Kang, A review on mixing in microfluidics, Micromachines 1 (2010) 82–111.
[11] C.-Y. Lee, W.-T. Wang, C.-C. Liu, L.-M. Fu, Passive mixers in microfluidic systems: A review, Chem. Eng. J. 288 (2016) 146–160.
[12] J. Green, A. Holdø, A. Khan, A review of passive and active mixing systems in microfluidic devices, Int. J. Multiphys. 1 (1) (2007) 1–32.
[13] I. Avramov, Relationship between diffusion, self-diffusion and viscosity, J. Non-Crystal. Solids 355 (10-12) (2009) 745–747.
[14] E. Rondeau, J.J. Cooper-White, Biopolymer microparticle and nanoparticle formation within a microfluidic device, Langmuir 24 (13) (2008) 6937–6945.
[15] Y. Xie, N.W. Todd, Z. Liu, M. Zhan, H. Fang, H. Peng, M. Alattar, J. Deepak, S. A. Stass, F. Jiang, Altered miRNA expression in sputum for diagnosis of non-small cell lung cancer, Lung Cancer 67 (2) (2010) 170–176.
[16] R.H. Liu, J. Yang, M.Z. Pindera, M. Athavale, P. Grodzinski, Bubble-induced acoustic micromixing, Lab Chip 2 (2002) 151–157.
[17] E. Choi, K. Kwon, S.J. Lee, D. Kim, J. Park, Non-equilibrium electrokinetic micromixer with 3D nanochannel networks, Lab Chip 15 (8) (2015) 1794–1798.
[18] Y. Wang, J. Zhe, B.T.F. Chung, P. Dutta, A rapid magnetic particle driven micromixer, Microfluid. Nanofluid. 4 (5) (2008) 375–389.
[19] G.-P. Zhu, N.-T. Nguyen, Rapid magnetofluidic mixing in a uniform magnetic field, Lab Chip 12 (2012) 4772–4780.
[20] K. Ward, Z.H. Fan, Mixing in microfluidic devices and enhancement methods, J. Micromech. Microeng. 25 (9) (2015), 094001.
[21] G. Destgeer, H.J. Sung, Recent advances in microfluidic actuation and micro-object manipulation via surface acoustic waves, Lab Chip 15 (2015) 2722–2738.
[22] M. Wiklund, Acoustofluidics 12: Biocompatibility and cell viability in microfluidic acoustic resonators, Lab Chip 12 (2012) 2018–2028.
[23] M. Stringer, Z. Zeng, X. Zhang, Y. Chai, W. Li, J. Zhang, H. Ong, D. Liang, J. Dong, Y. Li, Methodologies, technologies, and strategies for acoustic streaming-based acoustofluidics, Appl. Phys. Rev. 10 (2023), 011315.
[24] R. Shilton, M.K. Tan, L.Y. Yeo, J.R. Friend, Particle concentration and mixing in microdrops driven by focused surface acoustic waves, J. Appl. Phys. 104 (1) (2008).
[25] T. Frommelt, M. Kostur, M. Wenzel-Schäfer, P. Talkner, P. Hänggi, A. Wixforth, Microfluidic mixing via acoustically driven chaotic advection, Phys. Rev. Lett. 100 (2008), 034502.
[26] A.M. Gracioso Martins, N.R. Glass, S. Harrison, A.R. Rezk, N.A. Porter, P. D. Carpenter, J. Du Plessis, J.R. Friend, L.Y. Yeo, Toward complete miniaturisation of flow injection analysis systems: microfluidic enhancement of chemiluminescent detection, Anal. Chem. 86 (2014) 10812–10819.
[27] J.-C. Hsu, C.-Y. Chang, Enhanced acoustofluidic mixing in a semicircular microchannel using plate mode coupling in a surface acoustic wave device, Sens. Actuators, A 336 (2022), 113401.
[28] W. Wei, Y. Wang, Z. Wang, X. Duan, Microscale acoustic streaming for biomedical and bioanalytical applications, TrAC Trends Anal. Chem. 160 (2023) 116958.
[29] X. Luo, J. Cao, H. Gong, H. Yan, L. He, Phase separation technology based on ultrasonic standing waves: A review, Ultrason. Sonochem. 48 (2018) 287–298.
[30] M. Wiklund, R. Green, M. Ohlin, Acoustofluidics 14: Applications of acoustic streaming in microfluidic devices, Lab Chip 12 (2012) 2438–2451.
[31] J. Nam, C.S. Lim, Micromixing using swirling induced by three-dimensional dual surface acoustic waves (3D-dSAW), Sens. Actuators B 255 (2018) 3434–3440.
[32] J. Park, G. Destgeer, M. Afzal, H.J. Sung, Acoustofluidic generation of droplets with tunable chemical concentrations, Lab Chip 20 (2020) 3922–3929.
[33] Y. Im, S. Kim, J. Park, H.J. Sung, J.S. Jeon, Antibiotic susceptibility test under a linear concentration gradient using travelling surface acoustic waves, Lab Chip 21 (2021) 3449–3457.
[34] H. Ahmed, G. Destgeer, J. Park, J.H. Jung, H.J. Sung, Vertical hydrodynamic focusing and continuous acoustofluidic separation of particles via upward migration, Adv. Sci. 5 (2018), 1700285.
[35] H. Ahmed, J. Park, G. Destgeer, M. Afzal, H.J. Sung, Surface acoustic wave-based micromixing enhancement using a single interdigital transducer, Appl. Phys. Lett. 114 (2019), 043702.
[36] Y. Kazama, E.T. Carlen, A. van den Berg, A. Hibara, Top-and-side dual-view microfluidic device with embedded prism, Sens. Actuators B 248 (2017) 753–760.
[37] M.B. Dentry, L.Y. Yeo, J.R. Friend, Frequency effects on the scale and behavior of acoustic streaming, Phys. Rev. E 89 (2014), 013203.
[38] D.J. Collins, Z. Ma, J. Han, Y. Ai, Continuous micro-vortex-based nanoparticle manipulation via focused surface acoustic waves, Lab Chip 17 (2017) 91–103.
[39] D.J. Collins, Z. Ma, Y. Ai, Highly localized acoustic streaming and size-selective submicrometer particle concentration using high frequency microscale focused acoustic fields, Anal. Chem. 88 (2016) 5513–5522.

[40] J. Park, J.H. Jung, K. Park, G. Destgeer, H. Ahmed, R. Ahmad, H.J. Sung, On-demand acoustic droplet splitting and steering in a disposable microfluidic chip, Lab Chip 18 (2018) 422–432.

[41] J.M. Ottino, Mixing, chaotic advection, and turbulence, Annu. Rev. Fluid Mech. 22 (1990) 207–254.

[42] X. Niu, L. Liu, W. Wen, P. Sheng, Active microfluidic mixer chip, Appl. Phys. Lett., 88 (2006) 153508 https://doi.org/10.1063/1.2195567.

[43] B. Cha, W. Kim, G. Yoon, H. Jeon, J. Park, Enhanced solutal Marangoni flow using ultrasound-induced heating for rapid digital microfluidic mixing, Front. Phys. 9 (2021), 735651.

[44] M.R. Rasouli, M. Tabrizian, An ultra-rapid acoustic micromixer for synthesis of organic nanoparticles, Lab Chip 19 (2019) 3316–3325.

[45] M.C. Jo, R. Guldiken, Dual surface acoustic wave-based active mixing in a microfluidic channel, Sens. Actuators, A 196 (2013) 1–7.

[46] J. Carr, RF components and circuits, Newnes, 2002.

[47] B.H. Ha, K.S. Lee, G. Destgeer, J. Park, J.S. Choung, J.H. Jung, J.H. Shin, H.J. Sung, Acoustothermal heating of polydimethylsiloxane microfluidic system, Sci. Rep. 5 (2015) 11851.

[48] A.D. Anastasiou, A.S. Spyrogianni, K.C. Koskinas, G.D. Giannoglou, S.V. Paras, Experimental investigation of the flow of a blood analogue fluid in a replica of a bifurcated small artery, Med. Eng. Phys. 34 (2012) 211–218.

[49] M. Lin, T. Tsai, Y. Yang, Measurement of viscosity of human semen with a rotational viscometer, J. Formosan Med. Assoc. Taiwan yi zhi 91 (1992) 419–423.

[50] N.-S. Cheng, Formula for the viscosity of a glycerol− water mixture, Ind. Eng. Chem. Res. 47 (2008) 3285–3288.

[51] C. Westerhausen, L.G. Schnitzler, D. Wendel, R. Krzysztoń, U. Lächelt, E. Wagner, J.O. Rädler, A. Wixforth, Controllable acoustic mixing of fluids in microchannels for the fabrication of therapeutic nanoparticles, Micromachines 7 (2016) 150.

[52] S. Orbay, A. Ozcelik, J. Lata, M. Kaynak, M. Wu, T.J. Huang, Mixing high-viscosity fluids via acoustically driven bubbles, J. Micromech. Microeng. 27 (2016), 015008.

[53] Z. Wang, P.-H. Huang, C. Chen, H. Bachman, S. Zhao, S. Yang, T.J. Huang, Cell lysis via acoustically oscillating sharp edges, Lab Chip 19 (2019) 4021–4032.

[54] M. Shehadul Islam, A. Aryasomayajula, P.R. Selvaganapathy, A review on macroscale and microscale cell lysis methods, Micromachines 8 (2017) 83.

[55] R.B. Brown, J. Audet, Current techniques for single-cell lysis, J. R. Soc. Interface 5 (2008) S131–S138.

[56] J. Gao, X.-F. Yin, Z.-L. Fang, Integration of single cell injection, cell lysis, separation and detection of intracellular constituents on a microfluidic chip, Lab Chip 4 (2004) 47–52.

[57] H. Lu, K. Mutafopulos, J.A. Heyman, P. Spink, L. Shen, C. Wang, T. Franke, D. A. Weitz, Rapid additive-free bacteria lysis using traveling surface acoustic waves in microfluidic channels, Lab Chip 19 (24) (2019) 4064–4070.

[58] Z. Ramshani, C. Zhang, K. Richards, L. Chen, G. Xu, B.L. Stiles, R. Hill, S. Senapati, D.B. Go, H.-C. Chang, Extracellular vesicle microRNA quantification from plasma using an integrated microfluidic device, Commun. Boil. 2 (2019) 189.

[59] E. de la Serna, K. Arias-Alpízar, L.N. Borgheti-Cardoso, A. Sanchez-Cano, E. Sulleiro, F. Zarzuela, P. Bosch-Nicolau, F. Salvador, I. Molina, M. Ramirez, Detection of Plasmodium falciparum malaria in 1 h using a simplified enzyme-linked immunosorbent assay, Anal. Chim. Acta 1152 (2021), 338254.

[60] S. Himbert, R.J. Alsop, M. Rose, L. Hertz, A. Dhaliwal, J.M. Moran-Mirabal, C. P. Verschoor, D.M.E. Bowdish, L. Kaestner, C. Wagner, M.C. Rheinstädter, The molecular structure of human red blood cell membranes from highly oriented, solid supported multi-lamellar membranes, Sci. Rep. 7 (1) (2017).

[61] V. Gómez Flores, A. Martínez-Martínez, J.A. Roacho Pérez, J. Acosta Bezada, F. S. Aguirre-Tostado, P.E. García Casillas, Biointeraction of erythrocyte ghost membranes with gold nanoparticles fluorescents, Materials 14 (2021) 6390.

[62] Q. Ramadan, V. Samper, D. Poenar, Z. Liang, C. Yu, T. Lim, Simultaneous cell lysis and bead trapping in a continuous flow microfluidic device, Sens. Actuators B 113 (2006) 944–955.